energies

Article

Numerical and Experimental Investigation on a Moonpool-Buoy Wave Energy Converter

Hengxu Liu [1], Feng Yan [1], Fengmei Jing [2,*], Jingtao Ao [1], Zhaoliang Han [1] and Fankai Kong [3]

1 College of Shipbuilding Engineering, Harbin Engineering University, Harbin 150001, China; liuhengxu@hrbeu.edu.cn (H.L.); yanfeng413@hrbeu.edu.cn (F.Y.); edisonchai@hrbeu.edu.cn (J.A.); hanzhaoliang@hrbeu.edu.cn (Z.H.)
2 School of Mechanical Engineering, Beijing Institute of Petrochemical Technology, Beijing 100083, China
3 College of Mechanical and Electrical Engineering, Harbin Engineering University, Harbin 150001, China; kongfankai@hrbeu.edu.cn
* Correspondence: jingfengmei@hrbeu.edu.cn; Tel.: +86-1504-563-0022

Received: 8 April 2020; Accepted: 7 May 2020; Published: 9 May 2020

Abstract: This paper introduces a new point-absorber wave energy converter (WEC) with a moonpool buoy—the moonpool platform wave energy converter (MPWEC). The MPWEC structure includes a cylinder buoy and a moonpool buoy and a Power Take-off (PTO) system, where the relative movement between the cylindrical buoy and the moonpool buoy is exploited by the PTO system to generate energy. A 1:10 scale model was physically tested to validate the numerical model and further prove the feasibility of the proposed system. The motion responses of and the power absorbed by the MPWEC studied in the wave tank experiments were also numerically analyzed, with a potential approach in the frequency domain, and a computational fluid dynamics (CFD) code in the time domain. The good agreement between the experimental and the numerical results showed that the present numerical model is accurate enough, and therefore considering only the heave degree of freedom is acceptable to estimate the motion responses and power absorption. The study shows that the MPWEC optimum power extractions is realized over a range of wave frequencies between 1.7 and 2.5 rad/s.

Keywords: wave energy converter; moonpool; motion response; wave tank experiment

1. Introduction

Carbon emission from the use of fossil fuels is increasingly recognized as a worldwide concern [1]. Marine renewable energy was deemed a possible source of clean and sustainable energy, and had been widely studied over the past decades. Wave energy has unique advantages such as massive reserves, wide distribution, high energy density, and easy to exploit. The principle of wave energy utilization is to convert the kinetic energy and the potential energy of waves into the electrical energy through wave energy converters (WECs). In terms of the energy capture mode, the WEC devices can be divided into three types: oscillating water column devices, overtopping devices, and point-absorption wave energy converters (PAWEC) [2]. PAWEC uses the reciprocating motion in the six degrees of freedom to drive power take-off system and achieves the conversion process from wave energy to electrical energy. PAWECs have demonstrated some advantages over other WECs, such as a smaller volume and high wave energy conversion per unit volume [3]; PAWECs are also easy to realize in modules (and therefore easy to scale up), and to combine with floating structures [4]. The combination PAWEC systems with other ocean platforms (such as, for example, floating wind turbines) in hybrid platforms is starting to gain attraction [5]. One pioneer work is the Spar-Torus Combination (STC) (Figure 1a) concept developed by Muliawan [6]. The working principle of the STC device is to have a floating torus component, at waterline level, around the SPAR support platform of a wind turbine, and to exploit the relative motion between the wind turbine and the torus to generate electricity. Similar wind-wave hybrid devices are the Wind Lens [7] in Japan, the W2Power [8] (Figure 1b) in Norway, and the wind-wave hybrid platform [9] (Figure 1c). In addition to offshore wind turbines, semi-submersible platforms can also host a series of PAWECs, such as the Manchester Bobber [10] (Figure 1d), wave star [11]. There is a fully packed spheroidal smart buoy hybrid generator (SB-HG) composed of triboelectric nanogenerator (TENG) and an electromagnetic generator (EMG) [12,13]. Recently, a research group from Harbin Engineering University (Liu et al. [14]) filed a patent for the "Wave energy converter with funnel-shape moonpool structure" (Figure 1e), which has been granted (authorization code: ZL201610293268.8).

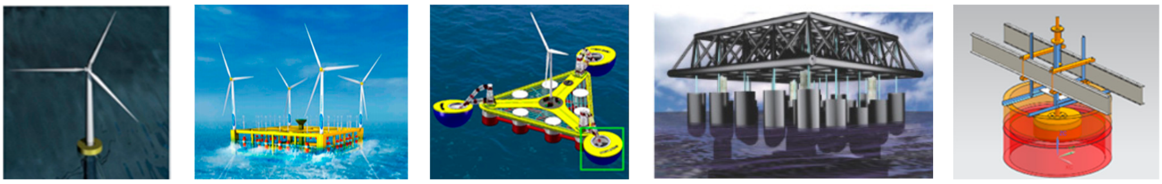

(**a**) (**b**) (**c**) (**d**) (**e**)

Figure 1. The typical ocean platform-point-absorption wave energy converters (PAWEC) devices. (**a**) Adapted from reference [6]; (**b**) Adapted from reference [8]; (**c**) Adapted from reference [9]; (**d**) Adapted from reference [10] and (**e**) Adapted from reference [14].

Compared with the research on single PAWECs, for multiple PAWECs integrated with other energy devices, the coupling effect between PAWEC and the platform needs to be considered. The numerical methods used usually adopt both frequency and time domain approaches [15]: the linear hydrodynamic properties are obtained using a potential flow solver in the frequency domain, and then the hydromechanics coefficients are used in the time domain through time delay function. Taghipour and Moan [16] researched a multiple WEC configuration, in the frequency domain, using a mode expansion method, to evaluate the performance of the WEC devices in converting the wave energy and its dynamic characteristic in ocean waves. Lee et al. [17] numerically simulated on the multi-body hydrodynamic interaction between a hybrid floating platform and a multi-wave energy converter, in the frequency domain. Since linear potential theory cannot capture viscous effects, usually empirical methods are adopted to include this effect, be it numerical or experimental. However, recent trends [18] in the development of CFD methods have shown increasing interests in modelling WECs, where viscous effects are non-ignorable. Lo et al. [19] used a CFD approach to analyze the performance of an air-blower wave energy converter, and to calculate the power output of two buoys. Jin et al. [20] took the nonlinear viscosity into account to model the WEC hydrodynamics near resonance conditions. Nonlinear PAWEC system's hydrodynamics, in conditions close to resonance (i.e., incident wave frequency near the systems' natural frequency) or in high wave heights conditions, can be realistically carried out. In order to reduce the computational costs linked to CFD methodologies, Liu et al. [21] introduced a nonlinear viscous dissipative term in the modelling the moonpool structure, and derived the relationship between the nonlinear dissipation coefficient and the resonant frequency of the moonpool.

Experimental methods are a useful way of carrying out feasibility studies of newly developed WECs. However, full-scale model tests at sea may be expensive and technically challenging, especially as a first step to validate a relatively new concept. A small-scale model test offers an alternative but effective way to tackle this problem. Zheng et al. [22] investigated the motion and energy conversion of a WEC with two bodies relayed on tank experiment, deriving that the maximum efficiency is obtained when the wave period, the PTO damping coefficient, and the mass ratio are optimally tuned. In the case of hybrid platform, for example, Ren et al. [23] analyzed a combined monopile hybrid floating platform and a multi-wave energy converter, and derived the optimum tuning of the PTO damping through the use of coordinated numerical and experimental analyses. Gao et al. [24] studied three floating wind-wave hybrid concepts (STC, SFC, and OWC), comparing their energy efficiency and economic feasibility. Wan et al. [25–27] studied green water phenomena of STC, and the model test was used to simulate these nonlinear phenomena as well as the survivability of the device in extreme sea conditions. Unlike for the STC [28], Chen et al. [29] introduced a high-power integrated generation unit for offshore wind power and ocean wave energy (W2P), and tested output power of energy conversion devices. There are several papers about some similar works on numerical and experimental analyses of different wave energy converter published in Energies. Chybowski et al. [30] used the ANSYS AQWAWB and AQWA method to simulate the behavior of the device's performance, and the experimental studies recorded the performance of the prototype device. Thomas et al. [31] applied a shallow artificial neural network (ANN) which is a kind of machine learning language to obtain optimal working times. Wu et al. [32] put forward a new computational fluid dynamic method to predict the hydrodynamic characteristic of the Duck WEC, the results of which agree well with the experimental results. Kong et al. [33] adopted a semi-analytical approach based on the potential flow to assess the wave energy efficiency of the moonpool platform WEC in the journal of Energies.

Kong studied the WEC by the potential flow approach and ignored the viscous effect, so the viscous dissipation coefficient and experimental model were applied in the paper. This paper aims at investigating a new ocean platform-WEC device, which combines a moonpool platform and a WEC (MPWEC) system. Basically, an external cylindrical shell houses an internal moonpool, and an axysymmetrical point-absorber buoy is placed in this moonpool: the relative displacement between the cylindrical shell and the device is used to converter power. The displacement and power of the MPWEC in regular waves have been researched by a series of experiments in the wave tank at Harbin Engineering University. As mentioned, the experimental results are then used to benchmark the potential flow method and the CFD method, which are developed to numerically simulate the dynamics of the MPWEC device in the frequency and time domains, respectively. A satisfactory agreement is obtained between the numerical and experimental results.

2. Model Description

2.1. Similar Conditions

In this test, since the wave loads acting on the MPWEC and their oscillatory nature are the most important factors to take into account, the similitude numbers considered are the Froude and Strouhal:

$$Fr = \frac{V_m}{\sqrt{gL_m}} = \frac{V_s}{\sqrt{gL_s}}, St = \frac{V_m T_m}{L_m} = \frac{V_s T_s}{L_s} \tag{1}$$

where V, T, and L represent characteristic velocity, characteristic period, and characteristic length; the subscript "m" represents the scale model physical quantity, and the subscript "s" represents the full scale physical quantity. According to the above similarity criterions, Table 1 shows the original and scaled parameters applied in this study, a 1:10 geometrical scale factor was used.

2.2. Single Buoy

The single buoy, representing the body at the center of the moonpool, consists of a cylinder and a cylindrical cone in Figure 2. The upper cylinder has a of height 180 mm and diameter 750 mm, while the bottom cylindrical cone has a height 80 mm and diameter 750 mm. Accordingly, the prototype model has a height 1.8 m and diameter 7.5 m. The single buoy is connected to the sliding bearing system, attached on the beam of the cylindrical shell housing the moonpool, through the sliding shaft located in the middle of the single buoy (see Figure 2b).

Table 1. The scale comparison.

Variables	Entity Symbol	Model Symbol	Scale Factor	Scale Factor
Length	L_s	L_m	$L_s/L_m = \lambda$	10
Area	A_s	A_m	$A_s/A_m = \lambda^2$	100
Volume	V_s	V_m	$V_s/V_m = \lambda^3$	1000
Fluid density	ρ_s	ρ_m	$\rho_s/\rho_m = \gamma$	1.025
Displacement	Δ_s	Δ_m	$\Delta_s/\Delta_m = \gamma\lambda^3$	1025
Wave period	T_s	T_m	$T_s/T_m = \lambda^{1/2}$	3.15
Wave circular frequency	ω_s	ω_m	$\omega_s/\omega_m = \lambda^{-1/2}$	0.32
Velocity	v_s	v_m	$v_s/v_m = \lambda^{1/2}$	3.15
Acceleration	a_s	a_m	$a_s/a_m = 1$	1
Power	P_s	P_m	$P_s/P_m = \gamma\lambda^{3.5}$	3241.3

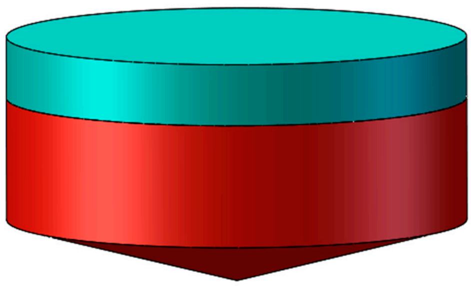

(**a**) Three-dimensional model

(**b**) view of the single buoy

Figure 2. The three-dimensional model and photography of single buoy.

2.3. *Moonpool-Buoy (Cylindrical Shell Housing the Moonpool)*

The moonpool-buoy consists of two cylindrical shells, closed at the bottom by a horizontal ring (Figure 3a,b). The inner and outer diameters of the moonpool-boy are, respectively, 1500 and 1600 mm. The total height of the moonpool-buoy is 991 mm, with a designed draft of 593 mm. Accordingly, the prototype model has an inner diameter 15 m, outer diameter 16 m, as well as draft 5.93 mm. A linear motor is fixed on the upper yellow beam (Figure 3b), and therefore it will not move with the wave, but the central cylindrical buoy oscillates in heave due to the waves occurring in the internal moonpool, and this motion is transmitted to the linear motor to produce energy.

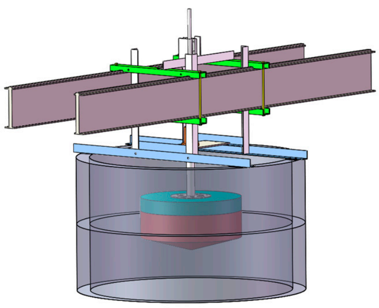

(**a**) Three-dimensional model (numerical simulation)

(**b**) Three-dimensional model (model test).

Figure 3. Moonpool-buoy device: on the left, 3D Computer Aided Design (CAD) schematics, with the central float in blue and red, the outer cylindrical shell in grey, and the connections to the above structure. On the right, a picture of the device in the tank.

2.4. The Data Acquisition System

The data collector was mainly used to collect voltage and current signals in Figure 4a. In this case, the voltage signal is mainly a linear motor and the rest of the line displacement sensors are all current signals. The data collector has eight channels to collect the electrical signals of eight sensors at the same time, the acquisition frequency meter is 100 Hz, the output power supply is 24 V, and the voltage measurement range is 0–10 V.

A linear displacement sensor was chosen, KTC1 gm rod sensor for measuring the displacement, the relative displacement ranges from 200 to 550 mm, pull rod length is 550 mm, the shell length is 628.5 mm, and the resolution is 0.01 mm. The maximum load pull is 50 kg, maximum speed is 10 m/s, the connection way is universal joints, and signal output type is the electric current.

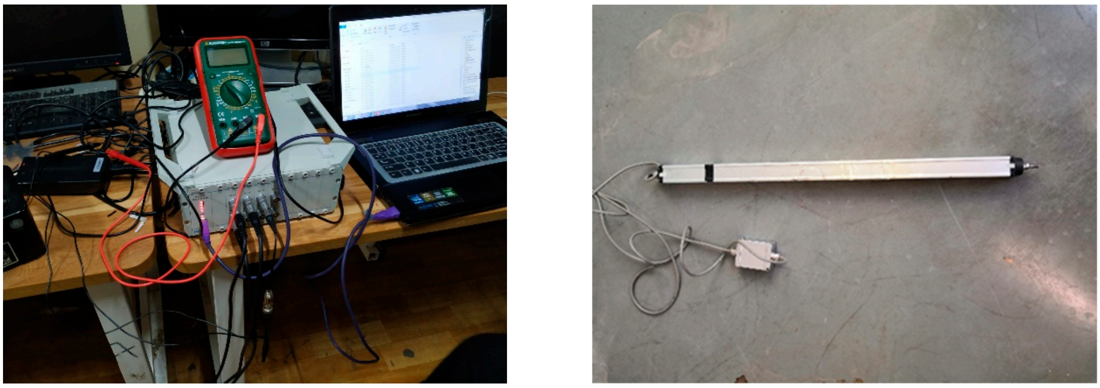

(**a**) The data collector (**b**) the line displacement sensor

Figure 4. The test measuring equipment.

3. Numerical Approach

The following section is about the numerical approach based on the potential flow method, which was used in this research. The potential flow method is to obtain the frequency domain results, and the RANS equation is to obtain the time domain results.

3.1. Potential Flow Method

Assuming that the balance is set in calm water, and the relative displacement is distance between the instantaneous position and equilibrium position. The motion equation of MPWEC device based on Newton's second law can be expressed as:

$$\begin{aligned} M_M \ddot{Z}_M &= F_M^E + F_{MM}^R + F_{MB}^R + F_M^K + F^P \\ M_B \ddot{Z}_B &= F_B^E + F_{BB}^R + F_{BM}^R + F_B^K + F^P \end{aligned} \tag{2}$$

where M_m, M_B represent the mass of moonpool and the wave energy buoy (WEB), respectively; Z_M, Z_B represent the displacement; F_M^E, F_B^E represent the wave load, the subscripts M and B are moonpool and the WEB, respectively, $F_{MM}^R, F_{MB}^R, F_{BB}^R, F_{BM}^R$ represent the radiation force the subscript *MM, MB, BB*, and *BM* are moonpool on itself, moonpool on the WEB, WEB on itself, and the WEB on the MP, which can be written as:

$$\begin{aligned} F_{MM}^R &= -\mu_{MM} \ddot{Z}_M - \lambda_{MM} Z_M; \; F_{MB}^R = -\mu_{MB} \ddot{Z}_B - \lambda_{MB} Z_B \\ F_{BM}^R &= -\mu_{BM} \ddot{Z}_M - \lambda_{BM} Z_M; \; F_{BB}^R = -\mu_{BB} \ddot{Z}_B - \lambda_{BB} Z_B \end{aligned} \tag{3}$$

where μ, λ represent the added mass and damping coefficient, respectively.

F_M^K, F_B^K represent the hydrostatic restoring force which can be expressed as:

$$F_M^K = k_M Z_M;\ F_B^K = k_B Z_B \tag{4}$$

where k_M, k_B represent static water restoring stiffness, when the waterline area S_j is constant, which can be expressed as $(k_M, k_B) = \rho g S_j$, where ρ and g are sea water density and gravitational acceleration, respectively. F^P is the PTO force, which can be expressed as the damping force associated with the relative velocity between the two bodies, as follows:

$$F^P = -c(Z_M - Z_B) \tag{5}$$

Assuming that wave is linear, by substituting Equations (3)–(5) into the equation, the motion equation can be further written as:

$$\begin{aligned} (M_M + \mu_{MM})\ddot{Z}_M + \mu_{MB}\ddot{Z}_B + \lambda_{MM}Z_M + \lambda_{MB}Z_B + c(Z_M - Z_B) + k_M Z_M = F_M^E \\ (M_B + \mu_{BB})\ddot{Z}_B + \mu_{BM}\ddot{Z}_M + \lambda_{BM}Z_M + \lambda_{BB}Z_B + c(Z_B - Z_M) + k_B Z_B = F_B^E \end{aligned} \tag{6}$$

where the hydrodynamic coefficient can be calculated by the Hydrostar software [34].

The moonpool and WEB can be connected by PTO damping system, the power can be expressed as:

$$\overline{P} = \frac{1}{2}\mathrm{Re}\Big[F^P(-i\omega(Z_M - Z_B))^*\Big] \tag{7}$$

where ω is incident wave frequency, Z_M, Z_B represent the motion amplitude of the MP and the WEB, and F^p is the PTO damping force.

Substituting Equation (5) into Equation (7)

$$\overline{P} = \frac{1}{2}c\omega^2(Z_M - Z_B)(Z_M - Z_B)* \tag{8}$$

where ω is incident wave frequency, Z_M, Z_B represent the motion amplitude, and c is the PTO damping coefficient.

3.2. RANS Method

The continuity equation and the Navier–Stokes equation can be described in the incompressible flow field [35]

$$\begin{aligned} \nabla \cdot \mathbf{U} = 0 \\ \rho\Big(\frac{\partial \mathbf{U}}{\partial t} + \mathbf{U} \cdot \nabla\mathbf{U}\Big) = -\nabla p + \mathbf{F}_b + \mu\nabla^2\mathbf{U} \end{aligned} \tag{9}$$

where ρ is the water density, $\mathbf{U}$ is the flow velocity vector, $\mathbf{F}_b$ is the body force vector, and μ is the dynamic viscosity coefficient. Starting from Navier–Stokes equations, and imposing the continuity equation, the Cauchy momentum equation can be derived. Then, assuming that the water density ρ is constant in space (incompressible) and in time, Expression (9) is obtained.

An CFD model based on RANS method (Star-CCM+) [36] is used to simulate fluid flow, where the finite volume method was applied in a computational mesh by discretizing the governing equations. A good agreement was found between the numerical and experimental results in the article. The free surface was captured by a volume of fluid method (VOF), and the moving boundary between the liquid and the central can be represented by a mesh morphing model. The cell motion was handled by a Lagrangian–Eulerian. A SIMPLE-type algorithm (SIMPLE algorithm is based on staggered grid to solve differential equations [37]) is adopted to solve the system of equations.

3.2.1. Computational Domain and Boundary Conditions

Figure 5 shows the computational domain and domain boundaries in the Star-CCM+ model. In order to reduce computational cost, and exploiting the problem symmetry, only half of the domain was modelled. The computational domain is 108 m long, 7 m wide, and 1.5 m high. Regarding the boundary conditions (Figure 4), the seabed is at 1.5 m below the mean water surface, non-penetration and a no-slip boundary condition was imposed, and a 5th-order Stokes wave velocity profile was specified at the inflow. The pressure outlet is implemented at the outflow boundary. The geometry of CFD model of the moonpool buoy WEC is the same as experimental model. In this paper, the renormalization group (RNG) k-ε model is applied as the turbulence model.

The incident wavelength determined the grid size x along the wave propagation direction, and the wave height H adjusted the grid size z along the vertical direction. A 5th-order Stokes wave was set at a height of 1 m and a period of 17.5 s.

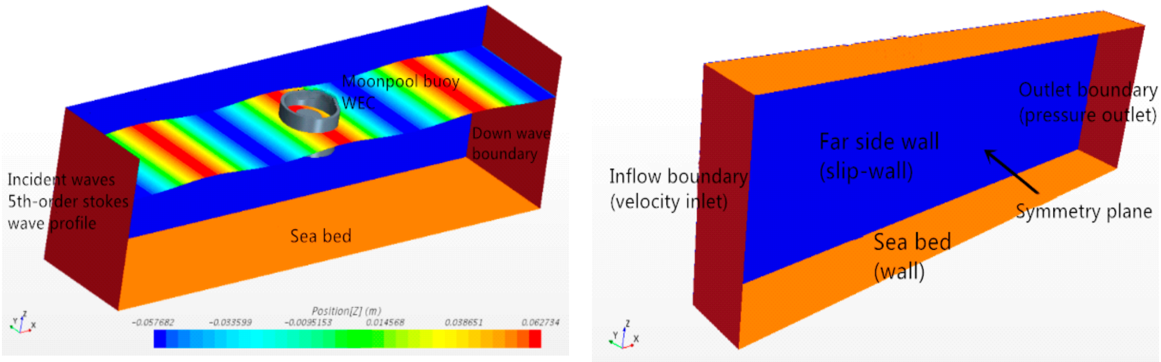

(**a**) the computational domain (**b**) the boundaries domian

Figure 5. Computational domain and domain boundaries.

3.2.2. Mesh Generation and Convergence Verification

The mesh was generated automatically by the automatic meshing facility in the Star-CCM+, which can result in 14 million cells in total in a computation mesh in Figure 6. The mesh generation can be applied to a trimmed cell mesher to produce a high-quality grid. Figure 6 shows the mesh of the moonpool-buoy WEC model. The grid resolution was enhanced near the free surface and around the model, to improve computational accuracy and capture the details of the flow around WEC and free surface. The different sizes of grids (d/60, d/45, and d/30, d is the draft of float) were applied to verify grid convergence, so the size d/30 was adopted to calculate more quickly in the exact case.

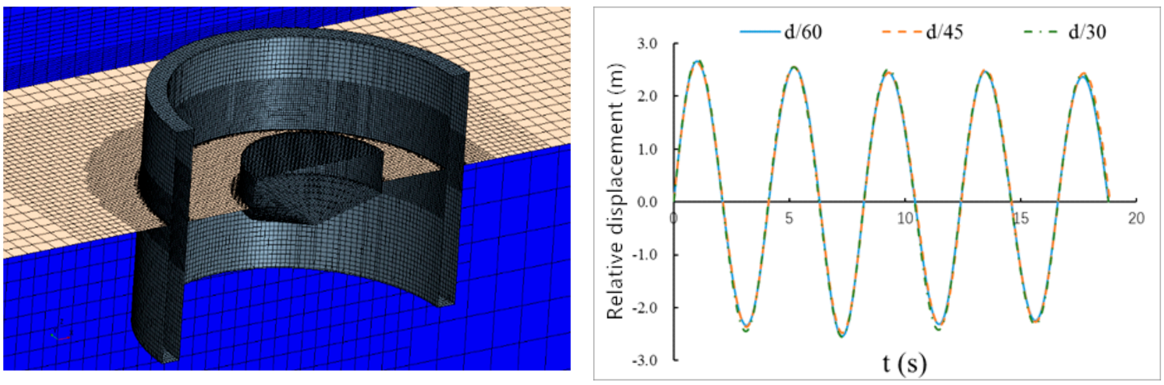

(**a**) mesh generation (**b**) mesh convergence

Figure 6. Grid around the moonpool-buoy wave energy converter (WEC) model convergence verification.

4. Experiments Process and Results

4.1. Experimental Facility

The experiments here considered were finished in the wave tank at HEU in Figure 7, having a length and width of 108 and 7 m, respectively. The depth of the test section is 1.5 m. The push-type wave generator can generate waves with a height up to 0.4 m and period between 0.4 and 4.0 s. The irregular waves that can be generated could model ITTC, JONSWAP, and P-M wave spectra with a wave height between 0 and 0.32 m.

(**a**) Towing tank (**b**) wave generator

Figure 7. Experimental facilities.

4.2. Wave Parameter

At first approximation, and under the conditions tested, it can be assumed that a linear relationship exists between the wave amplitude and the motion response of the tested device, and therefore the motion response amplitude operators can be defined (RAOs). The wave height is 0.12 m and the wave periods ranged from 1.2 to 3.0 s, as shown in Table 2. A total of 14 working conditions were considered in the model test.

Table 2. The working conditions.

Working Scenario Number	Wave Height (m)	Period (s)	Working Condition	Wave Height (m)	Period (s)
1	0.12	1.2	8	0.12	2.3
2	0.12	1.4	9	0.12	2.4
3	0.12	1.6	10	0.12	2.5
4	0.12	1.8	11	0.12	2.6
5	0.12	2.0	12	0.12	2.7
6	0.12	2.1	13	0.12	2.8
7	0.12	2.2	14	0.12	3.0

4.3. Single Buoy Model Test

4.3.1. Optimum Damping Coefficient

The damping coefficient of linear generator in the test model cannot be directly changed, so the PTO damping was changed, changing its electrical resistance in Figure 8. Its circuit diagram and the resistance box used are shown in Figure 8.

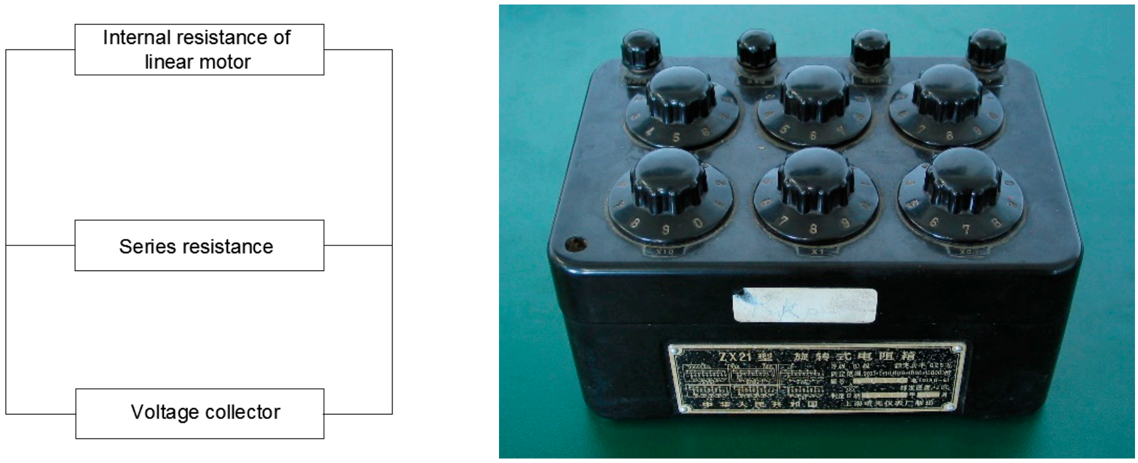

(**a**) the circuit diagram (**b**) the adjusting resistance

Figure 8. The circuit diagram and resistance box.

To determine the optimal damping, six resistance values were chosen (R_B = 5, 10, 20, 30, 40, and 50 Ω). The PTO damping characteristics change with the resistance due to the current intensity: the larger the resistance, the smaller the PTO damping.

It can be seen from Table 3 that the damping coefficient has a substantial impact on the output power. For example, for a monochromatic wave, the output power reaches maximum values when the resistance is 20 Ω. The relative displacement and power output are affected importantly by the PTO damping. There is an optimal damping to capture the maximal displacement and output power of WEC. Therefore, the PTO damping is optimal when the resistance value is 20 Ω to simplify the experimental workload.

Table 3. Output power with different resistances.

The Resistance of the Resistance Box (Ω)	Output Power (W)
5	0.56
10	0.80
20	0.97
30	0.95
40	0.87
50	0.79

4.3.2. Relative Motion and Power

The numerical results here presented were derived adopting a potential flow analysis method. At the same time, the viscous dissipation term was introduced to consider the actual sea conditions. The viscous dissipation coefficient can be expressed as ε, so the hydrodynamic coefficient can be written as

$$\begin{gathered} F = -i2\pi\rho g\xi_0(1-i\varepsilon)\int_{R_M}^{R_E}\varphi_{\ell=0}^{B}(r,-d_M)rdr \\ \mu + \frac{i\lambda}{\omega} = 2\pi\rho(1-i\varepsilon)\left\{\sum_{P=1}^{N}\int_0^{R_j}\varphi_1^{I_P}\left(r,h_p-h\right)rdr\right\} \end{gathered} \quad (10)$$

The wave period is in the range between 1.2 and 3.0 s, to be consistent with the experiment results relative displacement (Figure 8).

It can be seen from Figure 9 and Table 4 that there is a relatively good agreement between the trend of the numerical and experimental data. In general, the error between the numerical and experimental data is below 10% in absolute value, which can confirm the accuracy and suitability of the numerical approach. Anyway, since the viscous dissipation takes into account the potential viscous effects, there are lower errors expected when the wave period is 1.2 and 1.6 s due to the small period and the resonance period of the relative oscillation of the buoy in heave. The only notable discrepancies between the experimental data and the results of the numerical simulations were found at the resonance period of the floater, when the oscillation amplitude will be at its max level, and the numerical simulation underestimates the magnitude of the oscillation due to consideration of the viscous dissipation term.

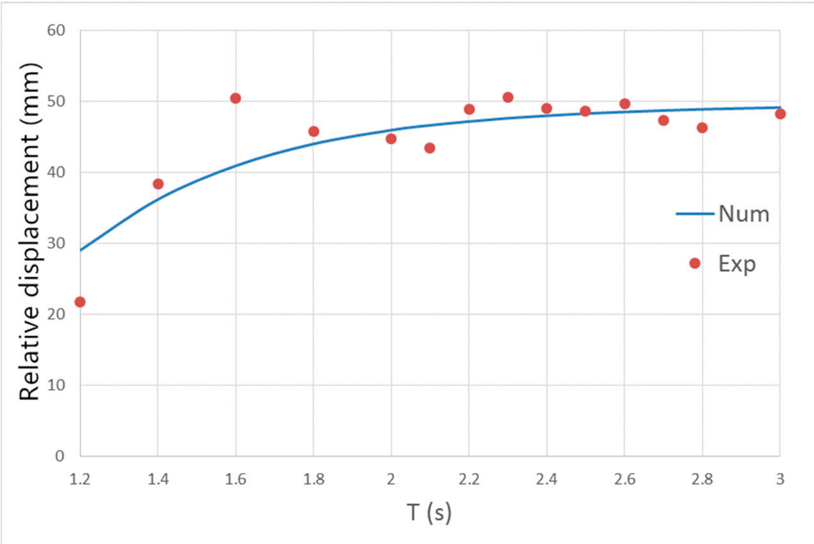

(**a**)

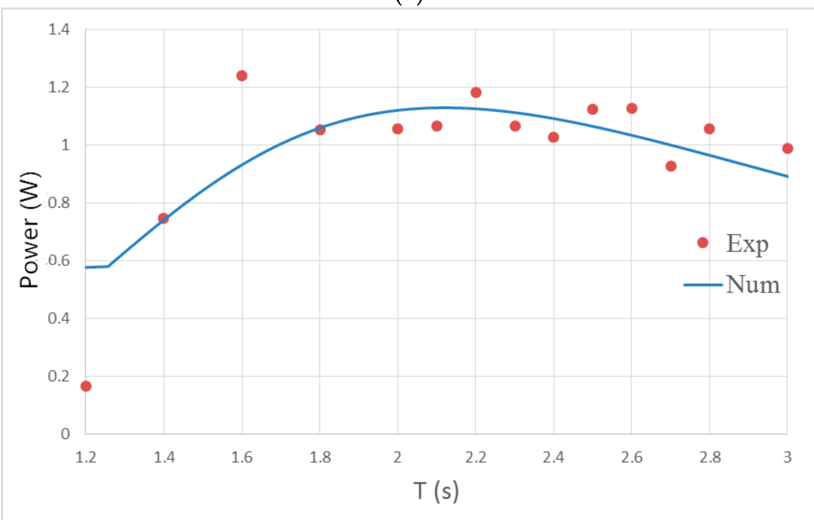

(**b**)

Figure 9. The motion curve and power curve in the different sea state: the continuous curve represents the numerical results obtained with a potential flow approach, and the points represent the experimental results. (**a**) Relative displacement (mm); (**b**) power output.

Table 4. Calculation error for oscillatory movement.

Wave Period (s)	Experimental Data (mm)	Numerical Data (mm)	Error Analysis (%)
1.2	21.8	29.0	33.1
1.4	38.4	36.2	5.8
1.6	50.4	40.9	18.9
1.8	45.7	44.0	3.9
2.0	44.7	45.9	2.7
2.1	43.4	46.6	7.4
2.2	48.8	47.1	3.5
2.3	50.5	47.6	5.7
2.4	49.0	47.9	2.1
2.5	48.7	48.3	0.8
2.6	49.6	48.5	2.3
2.7	47.3	48.7	2.9
2.8	46.3	48.8	5.5
3.0	48.2	49.1	1.8

4.4. Wave Tank Experiment for Moonpool-Buoy and Comparison with Numerical Results

4.4.1. The Moonpool Device

The device is composed of two parts, the moonpool cylindrical shell and the central float, as shown in Figure 3. The moonpool shell is set on the outside of the float and fixed on the trailer suspension bridge. The central float is connected to the linear motor by a shaft, and the linear motor is solidly fixed to the beam. The float, when subject to the wave loads, will incur a heaving oscillatory motion. The acceleration and the displacement are measured by sensors, and recorded by the data acquisition system. By postprocessing these data, is possible to derive the power absorbed by the device.

4.4.2. The Optimal Damping

To determine the optimal damping, we chose six resistance values, R_B = 5, 10, 20, 30, 40, and 50 Ω.

It can be seen from Table 5 that the damping coefficient has a substantial impact on the output power. The wave period is 1.8 s, which was randomly selected, when the resistance is 20 Ω.

Table 5. Output power with different resistances.

The Resistance of Resistance Box (Ω)	Output Power (W)
5	0.62
10	1.55
20	1.68
30	0.83
40	0.86
50	0.84

4.4.3. Motion Response and Power Output

Figure 10 below compares the numerical results with the added viscous dissipation coefficient (continuous lines) and the experimental results (points).

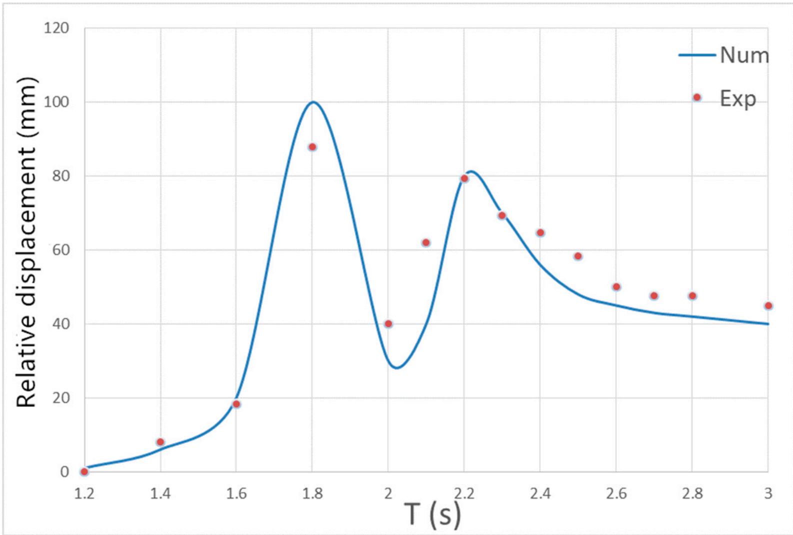

(**a**)

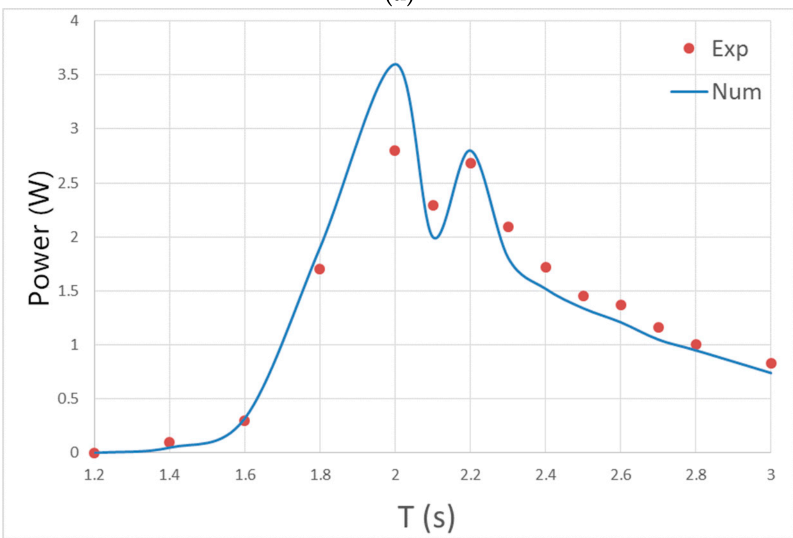

(**b**)

Figure 10. The motion and power comparison. (**a**) Relative displacement; (**b**) power output.

The experimental data and numerical results with the added viscous dissipation coefficient are shown and compared in Figure 10 and Table 6. It can be seen that, in general, most of differences between the experimental results and the numerical results are around 21% or lower except T = 2.0 and 2.1 s, but there is higher error when the wave period is 1.2 s due to the moonpool eliminate wave. A potential flow approach overestimates the oscillation, so the viscous dissipation was adopted by introducing coefficient $\varepsilon = 0.15$. However, at the resonant period, such as T = 2.0 and 2.1 s, the numerical data are less than the observed ones due to the viscous dissipation coefficient ($\varepsilon = 0.15$) that has a greater effect on the device. In addition, the motion response amplitude under the resonance period reaches 100 mm, which is significantly higher than the amplitude of 88 mm obtained in the experimental tests. Compared with Figure 8, the hydrodynamic performance of the moonpool float is superior to a single float under a certain periodic environment.

Table 6. Heave oscillation: error between the numerical and experimental data.

Wave Period (s)	Experimental Data (mm)	Numerical Data (mm)	Error Analysis (%)
1.2	0.0	1.0	100
1.4	8.0	6.3	21.3
1.6	18.2	20.5	12.6
1.8	88.0	100.4	14.1
2.0	40.0	30.5	23.8
2.1	62.0	40.5	34.7
2.2	79.5	80.4	1.1
2.3	69.5	70.7	1.7
2.4	64.7	56.8	12.2
2.5	58.3	48.2	17.3
2.6	50.1	45.1	10.0
2.7	47.7	43.3	9.2
2.8	47.7	42.6	10.7
3.0	45.0	40.3	10.4

4.4.4. Motion Response Comparation: Time Domain

The numerical results were derived using Star-CCM+ software, as explained in Section 3, to compare with the experimental data.

The comparison of the heave motion time histories and of the power extracted are shown in Figure 11 (taken period T = 2.0 s and T = 2.2 s). As it can be seen, after the initial transient response (from 0 to ≈10 s), the motion reaches the regime phase. By adopting the CFD RANS method described in the previous section, the viscous forces can be taken into account, and a much better agreement can be observed in terms of amplitude of oscillation. The CFD RANS approach illustrated in Section 3 can be then assumed to be a reliable numerical framework to assess the performance of the MPWEC device proposed.

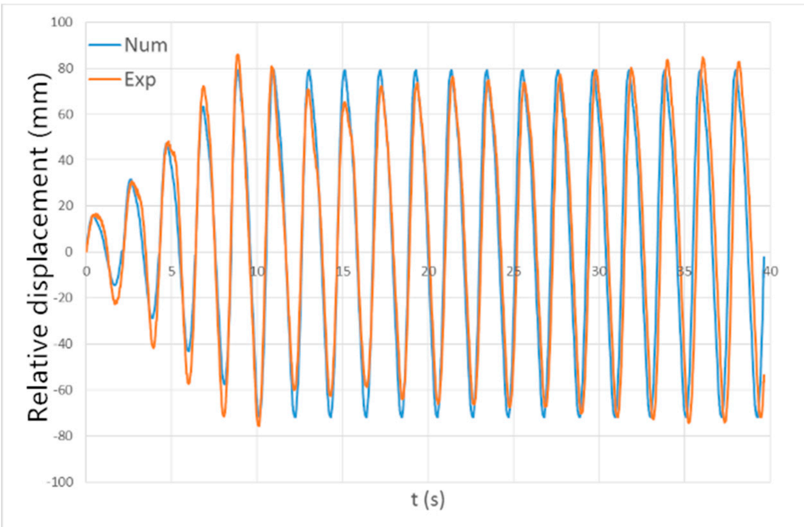

(a)

Figure 11. *Cont.*

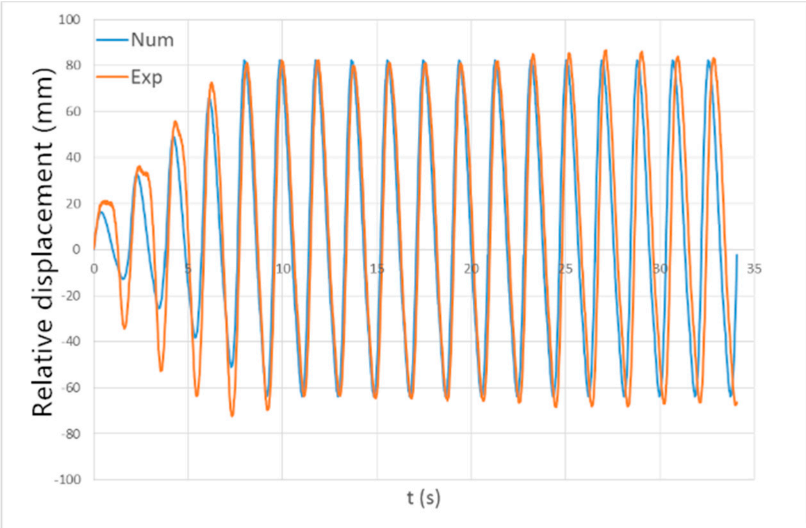

(b)

Figure 11. The motion comparison of the moonpool platform wave energy converter (MPWEC) with CFD results in time domain. (**a**) T = 2.0 s; (**b**) T = 2.2 s.

5. Conclusions

The research object is the moonpool float, and we developed moonpool float wave energy conversion device model design and test research, compared with the potential method and CFD method of the calculation results with the experimental measurements of the pool. We observed that wave period and PTO damping are important factors influencing the dynamic characteristic of WEC. Further research on moonpool float device of wave energy conversion and resonance characteristics is necessary in order to improve the moonpool float and the performance of the system as a whole on a technical and scientific basis.

The MPWEC with PTO system is presented in the article. Comparing all the above numerical and experimental results, the conclusions can be drawn as follows.

(1) The moonpool wave energy converter including moonpool and cylindrical buoy was designed. The experiment of a single buoy and moonpool buoy has resonant frequency with one and two resonant points, respectively. We observed that wave period and PTO damping are important factors that influence the wave energy converter's motion and energy extraction capability, according to the same experimental results.

(2) Either in the frequency domain or in the time domain, the experiment results and numerical results which were calculated by the potential method and CFD method has great agreement no more than 18.9%. Results showed that the efficiency of a single WEC reached the peak when the wave height was 0.12 m, wave period was 1.6 s, and the PTO damping corresponded to the resistance of 20 Ω. Results showed that the efficiency of MPWEC reached the peak when the wave height was 0.12 m, wave period was 1.8 and 2.2 s, and the PTO damping corresponded to the resistance.

(3) Compared with the single buoy and moonpool buoy, the moonpool can enhance the wave energy conversion in the frequency of 1.7–2.5 rad/s. On the contrary, when the wave period is short, the moonpool will hinder the motion of the cylinder buoy. It can be seen that the moonpool has wave elimination and wave gather.

In the future, the nonlinear PTO damping of wave energy device will be studied specially, and the optimal PTO damping coefficient will be determined. On this basis, the adaptive optimization algorithm of wave energy device can be further researched, and the control algorithm of PTO system can be explored in the time domain. The nonlinear wave theory will be applied to solve the complex hydrodynamic problems.

Author Contributions: Conceptualization, H.L.; methodology, F.Y. and F.J.; software, J.A.; validation, Z.H. and J.A.; writing—original draft preparation, J.A.; writing—review and editing, H.L.; funding acquisition, F.K. All authors have read and agreed to the published version of the manuscript.

Funding: This paper is financially supported by the National Natural Science Foundation (Grant No. 51979063 and U1706227), the basic research and cutting-edge technology projects of State Administration of Science (Grant NoJCKY2019604C003).

Conflicts of Interest: The authors declare no conflict of interest. The funders had no role in the design of the study; in the collection, analyses, or interpretation of data; in the writing of the manuscript, or in the decision to publish the results.

References

1. Patel, M.; Neelis, M.; Gielen, D.; Oliver, J.; Simmons, T.; Theunis, J. Carbon dioxide emissions from non-energy use of fossil fuels: Summary of key issues and conclusions from the country analyses. *Resour. Conserv. Recycl.* **2005**, *45*, 195–209. [CrossRef]
2. Cruz, J. Ocean Wave Energy: Current Status and Future Prespectives. *Bull. De Lacadémie Natl. De Médecine* **2008**, *196*, 1709–1720.
3. Chaplin, R.V.; Aggidis, G.A. An Investigation into Power from Pitch-Surge Point-Absorber Wave Energy Converters. In Proceedings of the IEEE ICCEP '07, International Conference on Clean Electrical Power, Capri, Italy, 21–23 May 2007.
4. Vicente, P.C.; de O. Falcã, A.F.; Gato, L.M.C.; Justino, P.A.P. Dynamics of arrays of floating point-absorber wave energy converters with inter-body and bottom slack-mooring connections. *Appl. Ocean Res.* **2009**, *31*, 267–281. [CrossRef]
5. Pérez-Collazo, C.; Greaves, D.; Iglesias, G. A review of combined wave and offshore wind energy. *Renew. Sustain. Energy Rev.* **2015**, *42*, 141–153. [CrossRef]
6. Muliawan, M.J.; Karimirad, M.; Moan, T.; Gao, Z. Stc (Spar-Torus Combination): A Combined Spar-Type Floating Wind Turbine and Large Point Absorber Floating Wave Energy Converter—Promising and Challenging. In Proceedings of the ASME 2012 31st International Conference on Ocean, Offshore and Arctic Engineering, Rio de Janeiro, Brazil, 1–6 July 2012; American Society of Mechanical Engineers: New York, NY, USA, 2012; pp. 667–676.
7. Ohya, Y.; Karasudani, T.; Nagai, T.; Watanabe, K. Wind lens technology and its application to wind and water turbine and beyond. *Renew. Energy Environ. Sustain.* **2017**, *2*, 2. [CrossRef]
8. Pelagic Power AS. W2Power Web Page. 2010. Available online: http://www.pelagicpower.no/ (accessed on 8 May 2020).
9. Lee, H.; Bae, Y.H.; Kim, K.H.; Park, S.; Hong, K. Influence of Second-Order Difference-Frequency Wave Loads on the Floating Wind-Wave Hybrid Platform. In Proceedings of the Asme International Conference on Ocean, Trondheim, Norway, 25–30 June 2017. [CrossRef]
10. Manchester Bobber wave power [Internet]. UK: REUK; c2006-16. 2015 December 18. Available online: http://www.reuk.co.uk/Manchester-Bobber-Wave-Power.htm (accessed on 29 January 2016).
11. Karimirad, M.; Koushan, K. WindWEC: Combining Wind and Wave Energy Inspired by Hywind and Wavestar. In Proceedings of the International Conference on Renewable Energy Research & Applications, Birmingham, UK, 20–23 November 2016. [CrossRef]
12. Arunkumar, C.; Venkateswaran, V.; Kim, S.-J. A fully packed spheroidal hybrid generator for water wave energy harvesting and self-powered position tracking. *Nano Energy* **2020**, *69*, 104439.
13. Chandrasekhar, A.; Vivekananthan, V.; Khandelwal, G.; Kim, S.-J. A Sustainable Blue Energy Scavenging Smart Buoy toward Self-Powered Smart Fishing Net Tracker. *ACS Sustain. Chem. Eng.* **2020**, *8*, 4120–4127. [CrossRef]
14. Liu, H.; Zhang, W. Wave energy converter with funnel-shape moonpool structure. Authorization code: ZL201610293268.8. Available online: http://cprs.patentstar.com.cn/Search/Detail?ANE=9EDA9DHB8HAA9GAD9EFB9HFD9FGE9BCD9IEG6AEAAGFA9HBH (accessed on 8 May 2020).
15. Borg, M.; Collu, M.; Brennan, F.P. Use of a Wave Energy Converter as a Motion Suppression Device for Floating Wind Turbines. *Energy Procedia* **2013**, *35*, 223–233. [CrossRef]

16. Taghipour, R.; Moan, T. Efficient Frequency-Domain Analysis of Dynamic Response of the Multi-Body Wave Energy Converter in Multi-Directional Waves. In Proceedings of the Eighteenth International Offshore and Polar Engineering Conference, Vancouver, CA, Canada, 6–11 July 2008.
17. Lee, H.; Poguluri, S.; Bae, Y. Performance Analysis of Multiple Wave Energy Converters Placed on a Floating Platform in the Frequency Domain. *Energies* **2018**, *11*, 406. [CrossRef]
18. Lee, H.; Bae, Y.H.; Cho, I.H.; Kim, K.H.; Hong, K. One-way Coupled Dynamic Analysis of Floating Platform with Wave Energy Converters. *J. Ocean Wind Energy* **2016**, *3*, 53–60. [CrossRef]
19. Lo, D.C.; Hsu, T.; Yang, C. Hydrodynamic Performances of Wave Pass Two Buoys-Type Wave Energy Converter. *Int. Soc. Offshore Polar Eng.* **2016**, 25–30, Accession number: 20175204583493.
20. Jin, S.; Patton, R.J.; Guo, B. Viscosity effect on a point absorber wave energy converter hydrodynamics validated by simulation and experiment. *Renew. Energy* **2018**, *129*, 500–512. [CrossRef]
21. Liu, H.-X.; Chen, H.-L.; Zhang, L.; Zhang, W.-C.; Liu, M. Quadratic Dissipation Effect on the Moonpool Resonance. *China Ocean Eng.* **2017**, *31*, 665–673. [CrossRef]
22. Zheng, X.; Yong, M.; Zhang, L.; Jiang, J.; Liu, H.-X. Experimental Investigation on the Hydrodynamic Performance of A Wave Energy Converter. *China Ocean Eng.* **2017**, *31*, 1–8. [CrossRef]
23. Ren, N.; Ma, Z.; Fan, T.; Zhai, G.; Ou, J. Experimental and numerical study of hydrodynamic responses of a new combined monopile wind turbine and a heave-type wave energy converter under typical operational conditions. *Ocean Eng.* **2018**, *159*, 1–8. [CrossRef]
24. Gao, Z.; Moan, T.; Wan, L.; Michailides, C. Comparative numerical and experimental study of two combined wind and wave energy concepts. *J. Ocean Eng. Sci.* **2015**, *1*, 36–51. [CrossRef]
25. Wan, L.; Greco, M.; Lugni, C.; Lugni, C.; Gao, Z.; Moan, T. A combined wind and wave energy-converter concept in survival mode: Numerical and experimental study in regular waves with a focus on water entry and exit. *Appl. Ocean Res.* **2017**, *63*, 200–216. [CrossRef]
26. Wan, L.; Gao, Z.; Moan, T. Experimental and numerical study of hydrodynamic responses of a combined wind and wave energy converter concept in survival modes. *Coast. Eng.* **2015**, *104*, 151–169. [CrossRef]
27. Wan, L.; Gao, Z.; Moan, T.; Lugni, C. Experimental and numerical comparisons of hydrodynamic responses for a combined wind and wave energy converter concept under operational conditions. *Renew. Energy* **2016**, *93*, 87–100. [CrossRef]
28. Liu, H. Stress analysis of the structural interface between the spar and the torus in the combined wind and wave energy concept STC. *Pol. Political Leg. Anthropol. Rev.* **1955**, *16*, 16–30.
29. Chen, W.; Gao, F.; Meng, X.; Chen, B.; Ren, A. W2P: A high-power integrated generation unit for offshore wind power and ocean wave energy. *Ocean Eng.* **2016**, *128*, 41–47. [CrossRef]
30. Chybowski, L.; Grządziel, Z.; Gawdzińska, K. Simulation and Experimental Studies of a Multi-Tubular Floating Sea Wave Damper. *Energies* **2018**, *11*, 1012. [CrossRef]
31. Wu, J.; Yao, Y.; Sun, D.; Ni, Z.; Göteman, M. Numerical and Experimental Study of the Solo Duck Wave Energy Converter. *Energies* **2019**, *12*, 1941. [CrossRef]
32. Thomas, S.; Eriksson, M.; Goyeman, M.; Hann, M.; Isberg, J.; Engström, J. Experimental and Numerical Collaborative Latching Control of Wave Energy Converter Arrays. *Energies* **2018**, *11*, 3036. [CrossRef]
33. Fankai, K.; Hengxu, L.; Weiming, S.; Jingtao, A.; Hailong, C.; Fengmei, J. Analytical and numerical analysis of the dynamics of a moonpool platform-wave energy buoy (MP-WEB). *Energies* **2019**, *10*, 21.
34. Xiaobo, C. Offshore hydrodynamics and applications. *Ies J. Part A Civ. Struct. Eng.* **2011**, *4*, 124–142.
35. Yu, Y.-H.; Li, Y. Reynolds-Averaged Navier–Stokes simulation of the heave performance of a two-body floating-point absorber wave energy system. *Comput. Fluids* **2013**, *73*, 104–114. [CrossRef]
36. Jing, Q. *A Simple Fluid Model for CFD Research Based on STAR-CCM+*; Hydraulics Pneumatics & Seals: Sichuan, China, 2010; Volume 30, pp. 8–10.
37. Patankar, S.V.; Spalding, D.B. A calculation procedure for heat, mass and momentum transfer in three-dimensional parabolic flows. *Int. J. Heat Mass Transf.* **1972**, *15*, 1787–1806. [CrossRef]